


Lensless high-resolution photoacoustic imaging scanner for in vivo skin imaging

Taiichiro Ida¹  · Hideaki Iwazaki¹ · Toshiyuki Omuro¹ · Yasushi Kawaguchi¹ · Yasuyuki Tsunoi² · Satoko Kawauchi² · Shunichi Sato²

Received: 12 July 2017 / Accepted: 16 October 2017 / Published online: 31 October 2017
© The Author(s) 2017. This article is an open access publication

Abstract We previously launched a high-resolution photoacoustic (PA) imaging scanner based on a unique lensless design for in vivo skin imaging. The design, imaging algorithm and characteristics of the system are described in this paper. Neither an optical lens nor an acoustic lens is used in the system. In the imaging head, four sensor elements are arranged quadrilaterally, and by checking the phase differences for PA waves detected with these four sensors, a set of PA signals only originating from a chromophore located on the sensor center axis is extracted for constructing an image. A phantom study using a carbon fiber showed a depth-independent horizontal resolution of $84.0 \pm 3.5 \mu\text{m}$, and the scan direction-dependent variation of PA signals was about $\pm 20\%$. We then performed imaging of vasculature phantoms: patterns of red ink lines with widths of 100 or 200 μm formed in an acrylic block co-polymer. The patterns were visualized with high contrast, showing the capability for imaging arterioles and venules in the skin. Vasculatures in rat burn models and healthy human skin were also clearly visualized in vivo.

Keywords Photoacoustic · In vivo imaging · Lensless · Phantom · Burn depth assessment

1 Introduction

Photoacoustic (PA) imaging, which is based on the optical absorption contrast mechanism, is a rapidly developing modality that enables anatomical and/or functional imaging for deep tissue. For high-resolution PA imaging, two representative schemes have been developed: optical resolution PA microscopy (OR-PAM) and acoustic resolution PA microscopy (AR-PAM). In OR-PAM, spatial resolution is determined by the focusing characteristics of an optical lens for PA excitation illumination, and a lateral resolution below 1 μm can be obtained [1–3]. However, the imaging depth is limited to less than 1 mm due to the strong light scattering effect in tissue. In AR-PAM, on the other hand, spatial resolution is determined by the focusing characteristics of an acoustic lens for PA signal collection, enabling imaging of deeper tissue [4–6]. AR-PAM is useful for full thickness skin imaging in medicine and cosmetology, but its horizontal resolution is decreased in defocused regions of the acoustic lens and compensation is needed [7], which may decrease imaging quality and accuracy. We previously launched a high-resolution PA imaging scanner based on a unique lensless design [8], but the details of the design and imaging algorithm were not disclosed. The design, imaging algorithm, and characteristics of the system are described in this paper.

2 Design, algorithm, and system

Figure 1 shows photographs of the PA scanning head, the arrangement of the ultrasound sensor (PZT) elements and optical fiber in the sensor unit, and the imaging principle. A compact stepping motor is mounted in the PA scanning head, enabling high-speed scanning at 40 $\mu\text{m}/\text{step}$. Four

✉ Taiichiro Ida
Taiichiro.ida@advantest.com

¹ New Concept Product Initiative, Advantest Corporation, 1-5, Shintone, Kazo, Saitama 349-1158, Japan

² Division of Bioinformation and Therapeutic Systems, National Defense Medical College Research Institute, 3-2, Namiki, Tokorozawa, Saitama 359-8513, Japan

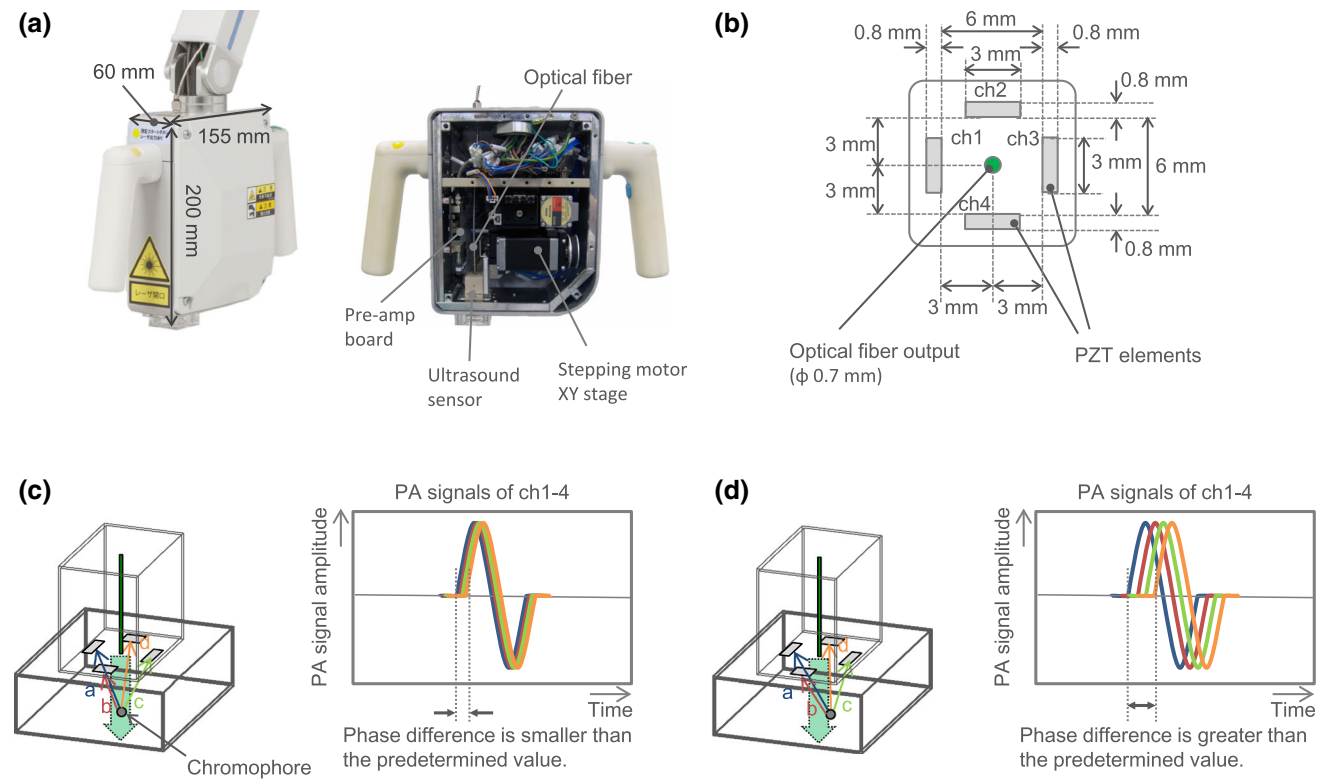


Fig. 1 **a** Photographs of the outside and inside of the PA scanning head. **b** Arrangement of the sensor elements and optical fiber in the sensor unit. **c** Illustrations of the imaging principle: position of the chromophore in relation to the imaging head (left) and difference in the phase or propagation time for PA signals detected with four sensor

elements (right). In the case of **c**, a chromophore is located on the sensor center axis. In the case of **d**, a chromophore is located out of the sensor center axis. The phase differences were compared with a predetermined very small value

0.8 mm × 3 mm PZT elements (ch 1–4; center frequency, 10 MHz) are arranged on the sides of the square, and the output end of an optical fiber of 0.7 mm in diameter for illumination is placed at the center of the square in the sensor unit. The PA wave originating from a chromophore is detected with four sensor elements, and the phases of four PA waves are checked. When a chromophore is located on the center axis of the sensor (i.e., the optical axis), the phases of four signals are the same (Fig. 1c). When a chromophore is located out of the center axis, on the other hand, the phases differ (Fig. 1d). Using only signals in the former case (Fig. 1c) for image construction, information on the sensor center axis can selectively be extracted, producing an image with a high horizontal resolution. In practice, the phase differences for a set of four signals ($\Delta\phi$) are compared with a predetermined very small value (hereafter simply called the value), and a set of PA signals for which phase differences are smaller than the value is only used for constructing an image. Schematics showing how the value is determined and the algorithm for imaging are shown in Fig. 2. We here assume that chromophores are located at a depth of 3 mm in a specimen. In this case, the distance between the chromophores and the

sensor bottom surface is 15 mm, since there is a water layer of 12 mm in thickness for PA signal coupling. We determined the value to selectively use PA signals generated from the chromophores that were located within a distance of 20 μm (half of the step size) from the optical fiber axis during a one-step (40 μm) scan of the sensor unit. In Fig. 2a, the top figure shows the situation in which a chromophore is located 20 μm from the fiber axis to the right side, and the bottom figure shows the sensor head that has moved a distance of one step (40 μm) to the right side and a chromophore is located 20 μm from the fiber axis to the opposite (left) side. These two figures indicate the limit of the region within which PA signals originating from chromophores are used for imaging for the scan direction. In these two cases, the difference in the two distances, the distance between the left sensor element (#1) and the chromophore (L1) and the distance between the right sensor element (#2) and the chromophore (L2), is calculated to be 9.70 μm . This corresponds to a phase difference in a time unit of 6.2 ns when a sound velocity of 1540 m/s is used. We used PA signals only when $\Delta\phi$ was smaller than this value (6.2 ns) for imaging. This criterion is valid for the other two sensor elements that are not shown in

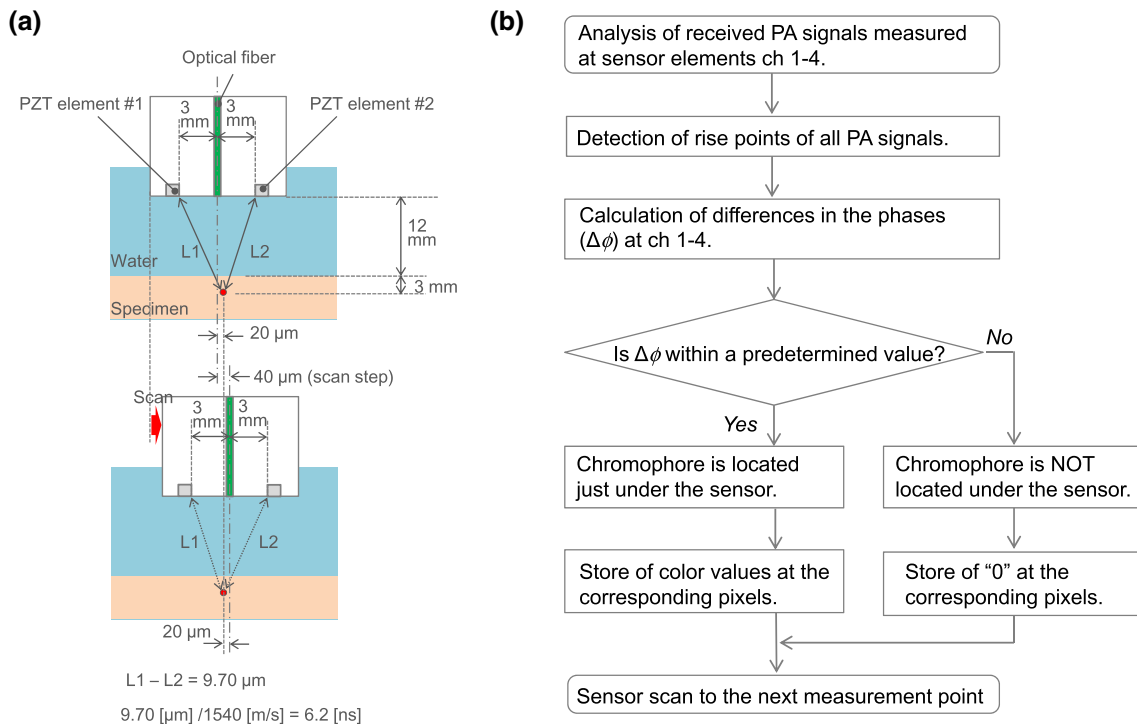


Fig. 2 a Illustrations showing how a predetermined value is determined. b Algorithm for imaging

Fig. 2a. In reality, however, 8 ns was used as the value, considering the sampling frequency of 250 Msps in the present system. In principle, this lensless high-resolution image construction mechanism is valid with three sensor elements, but a four-element scheme was used mainly due to the ease of fabrication of the sensor head.

A block diagram of the imaging system is shown in Fig. 3. The imaging head is mounted on a flexible arm, enabling measurements of various sites of the skin. The imaging head has a custom-designed XY scanning stage and a preamp board. Detected PA signals are amplified in the preamp board and sent to a field-programmable gate

array (FPGA) on a system board installed in the main frame. As a light source for PA excitation, a custom-made 532-nm Nd:YAG laser (pulse width, 2 ns FWHM; frequency, 1000 Hz) is also installed in the main frame, and output laser pulses are delivered to the imaging head through an optical fiber. The pulse energy is lower than 37 μJ/pulse, which satisfies the ANSI safety limit. The FPGA also controls the laser and the XY stage. The sensor unit is horizontally scanned on a resin spacer at 40-μm steps by the XY stage, and the scan time for a 4 mm × 4 mm area is about 20 s (laser frequency, 500 Hz) and that for 8 mm × 8 mm area is about 40 s (laser frequency, 1000 Hz). For imaging, the skin surface is placed under the resin spacer, and tissue is, therefore, not affected by motion of the sensor unit. Scanning, light emission, and signal capturing are synchronized by the FPGA. An obtained signal data set is sent from the FPGA to a PC through a USB interface. After measurement, it takes about 1 min to construct and display an image by the GPU.

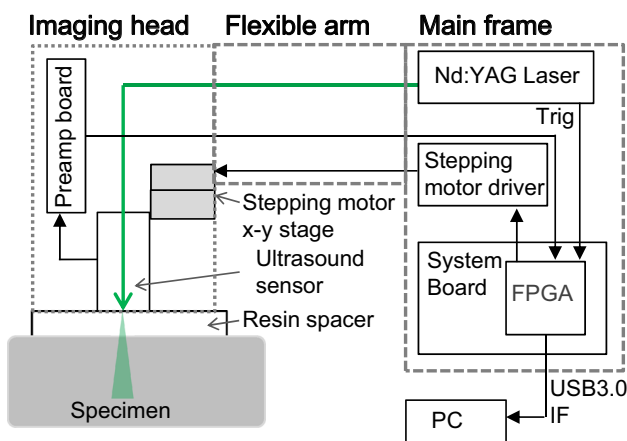


Fig. 3 Block diagram of the PA imaging system

3 Results and discussion

3.1 Phantom studies

We performed phantom studies to evaluate imaging characteristics of the system. As shown in Fig. 4a, a carbon fiber of 8 μm in diameter was placed horizontally at a

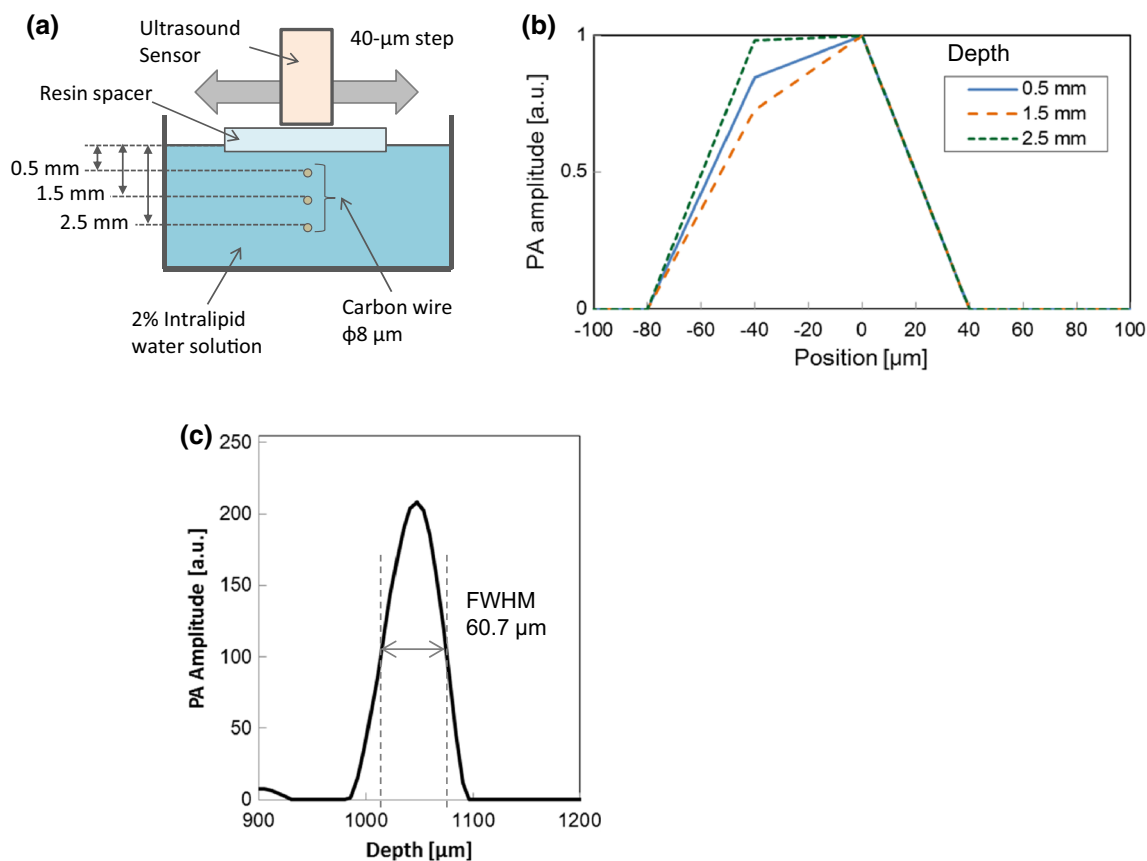


Fig. 4 Experimental setup and results of phantom studies: **a**, **b** carbon fibers in an Intralipid solution. **a** Setup for the PA measurements of carbon fibers. **b** Lateral distributions of peak PA signals originating

depth of 0.5, 1.5, or 2.5 mm in a 2% Intralipid water solution ($\mu_s' = 15 \text{ cm}^{-1}$), and the sensor head was scanned on the solution surface. Figure 4b shows lateral distributions of the peak amplitudes of PA signals at the three depths. The FWHM values were 83.6 μm at 0.5 mm, 87.5 μm at 1.5 mm, and 80.4 μm at 2.5 mm, indicating a depth-independent horizontal resolution of $84.0 \pm 3.5 \mu\text{m}$. Figure 4c shows a vertical direction profile of the PA signal obtained at a depth of 1.0 mm in the same solution. The FWHM value was 60.7 μm and the half wavelength corresponding to the PA signal frequency was calculated to be $\sim 104.7 \mu\text{m}$. Thus, the vertical resolution would be $\sim 100 \mu\text{m}$.

Due to the quadrilateral arrangement of the sensor elements, evaluation of the effect of the sensor head scanning direction on imaging characteristics would be important. With the same setup as that shown in Fig. 4a, a straight carbon fiber was rotated around the optical axis in steps of 15° (0° – 90°) on the horizontal plane, and the wire was imaged (Fig. 5a). Figure 5b shows lateral distributions of peak PA signals originating from a carbon fiber placed at a depth of 2.0 mm in the same solution. Direction-dependent variations of the PA signal amplitudes and FWHM values

from carbon fibers at different depths. **c** Vertical direction profile of the PA signal obtained at a depth of 1.0 mm in the same solution

were within about $\pm 20\%$ and $\pm 6.46 \mu\text{m}$, respectively, indicating the capability of isotropic imaging of the skin vasculature.

We then performed imaging of vasculature phantoms including two patterns of red ink lines formed in an acrylic block co-polymer: a rectangular mesh pattern with 200- μm -wide lines and a branch pattern with 200- and 100- μm -wide lines. The depths of the patterns were both 0.7 mm. Detailed optical and acoustic characteristics of the phantoms are reported in Ref. [9]. Both patterns, including a 1 mm x 1 mm square pattern (Fig. 6a) and 100- μm -wide branches (Fig. 6b), were visualized with high contrast, showing the capability for imaging arterioles and venues in the skin.

3.2 In vivo imaging

On the basis of the results of phantom studies, we attempted imaging of rat skin and human skin in vivo. Cross-sectional and 3D PA images were created from horizontal plane PA image data sets at 12.3- μm steps using the volume visualization software (VolView 3.4, Kitware, Inc.). All procedures for the animal experiment and

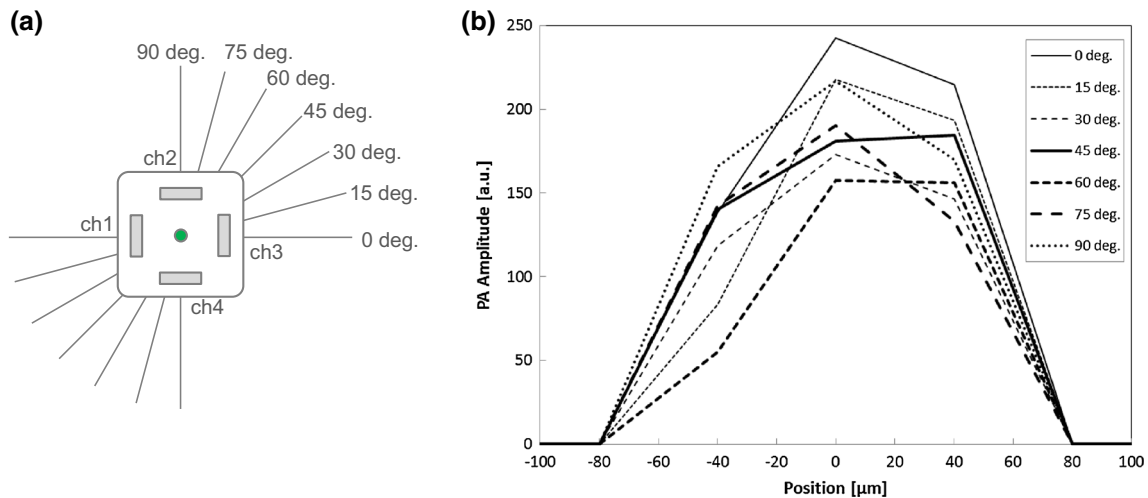
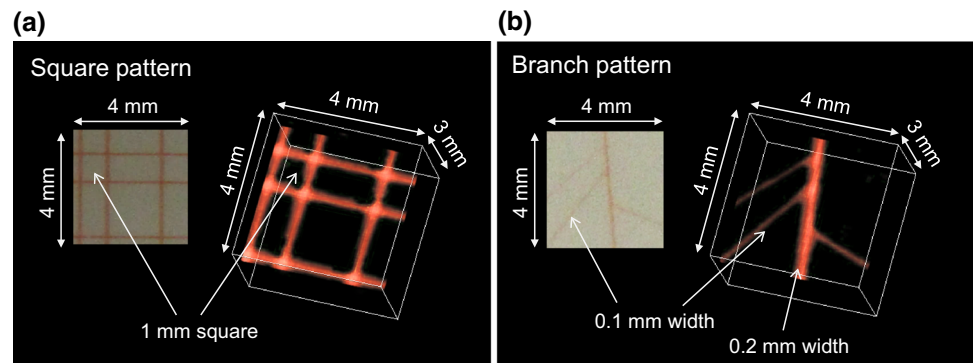


Fig. 5 Evaluation of the effect of the sensor head scanning direction on imaging characteristics for a carbon fiber in the Intralipid solution. **a** Rotating angles of a carbon fiber. **b** Lateral distributions of peak PA

signals originating from a carbon fiber placed at a depth of 2.0 mm for various rotating angles of the carbon fiber

Fig. 6 Imaging of vasculature-mimicking red ink line patterns formed in an acrylic block copolymer. **a** Mesh-pattern and **b** branch-pattern vasculature phantoms and their 3D PA images



measurements in human skin were approved by the Animal Care and Use Committee and the Medical Human Ethics Committee of the National Defense Medical College, respectively.

In the rat dorsal skin, we induced a deep dermal burn (DDB) and deep burn (DB) with a Walker–Mason template [10]. We previously developed a PA imaging system for burn depth assessment, by which PA signals originating from blood in the noninjured tissue layer under the injured tissue layer with vascular occlusion were detected, and we showed its validity by experiments using rat burn models [11, 12]. With that system, however, changes in the vascular structures were not detected due to the limitation in horizontal resolution. Figure 7 shows depth color-coded, cross-sectional and 3D PA images and the corresponding histological images with hematoxylin and eosin staining of (a) DDB and (b) DB at 24 h postburn. Surface signals, which are attributable to contamination and pigments in the epidermis, are shown by red in both the DDB and DB. In the 3D image of the DDB, vascular networks are shown by green and light blue, indicating viable vessels in the depth

range of 0.5–0.8 mm. In the 3D image of the DB, on the other hand, there are only vasculatures shown by blue, indicating viable vessels located deeper than 1 mm in the subcutaneous tissue. The depths of vasculatures visualized by PA imaging agreed well with the depths of viable blood vessels shown in the histological images of both the DDB and the DB. Information on the structure of vascular networks in wound beds would be useful for management and treatment of burn injuries.

Figure 8a, b shows a photograph of the imaging region (8 mm × 8 mm) of healthy human wrist skin and the corresponding 3D PA image, respectively. In the 3D image, the surface signal in the depth region of 0–1 mm is shown only for a quarter section of the horizontal area; strong surface signals (orange to red) are attributable to melanin in the epidermis. Under the strong surface signal, a thick blood vessel (vein) was observed at a depth of around 1 mm, and thinner vascular networks were also observed down to a region deeper than 2 mm, indicating the usefulness of the present imaging system for skin imaging not only in small animals but also in humans.

Fig. 7 Depth color-coded cross-sectional and 3D PA images of **a** DDB and **b** DB in rats at 24 h postburn and the corresponding histological images with hematoxylin and eosin staining. In histological images, scale bars indicate 200 μm and arrowheads show viable blood vessels

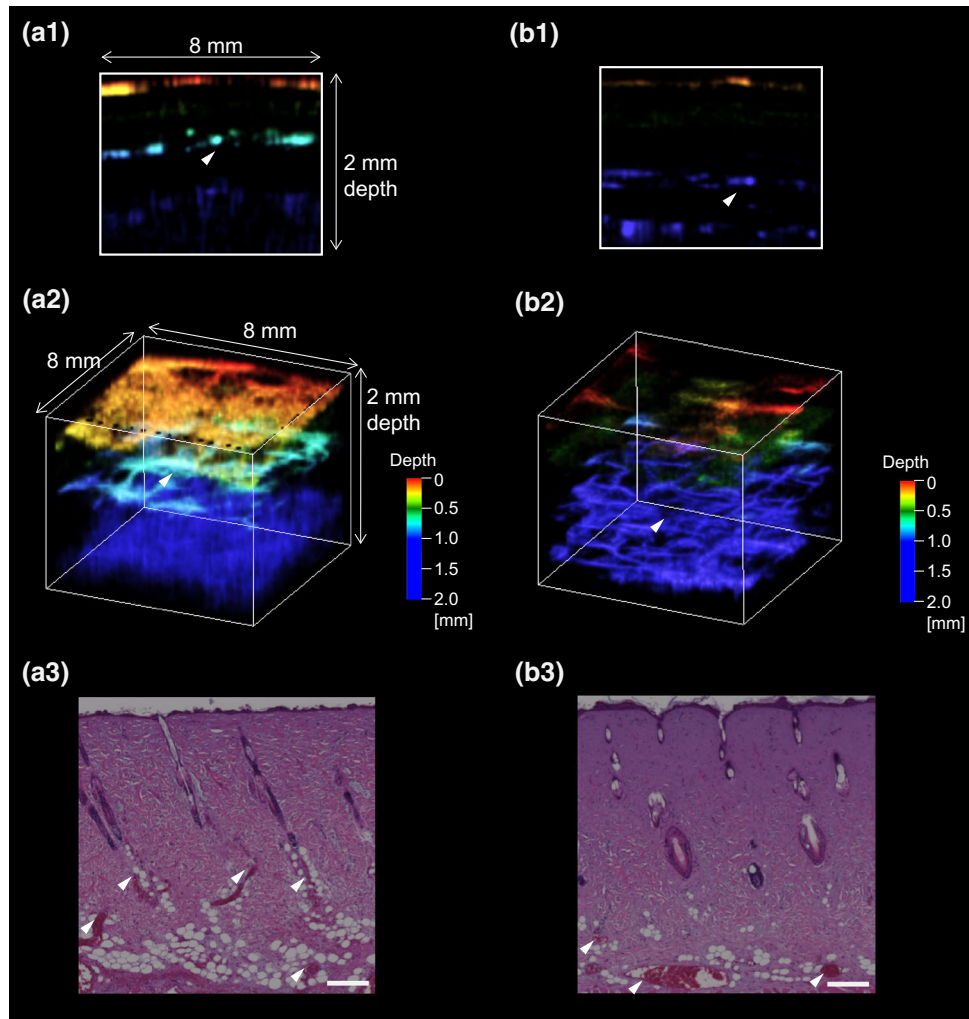
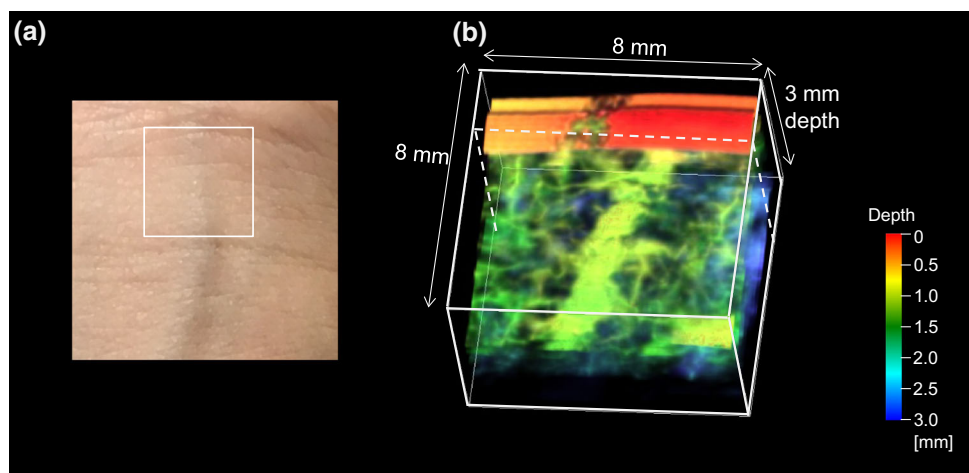


Fig. 8 **a** Photograph of the imaging region (8 mm \times 8 mm white line square) of healthy human wrist skin and **b** corresponding 3D PA image. In the PA image, surface signals in the depth range of 0–1 mm are shown only for a quarter section of the horizontal area



4 Conclusions

In summary, we developed a high-resolution photoacoustic imaging scanner for in vivo deep imaging of skin. Since neither an optical lens nor an acoustic lens is used in the

system, images obtained are free from the effects of defocusing. The flexible arm for the sensor head, as well as the scanning time of 40 s for an 8 mm \times 8 mm area, enables a wide range of in vivo skin imaging in dermatology, plastic surgery, and cosmetology.

Acknowledgements The authors thank Ms. Tsuyako Ohkura for skillful experimental assistance.

Open Access This article is distributed under the terms of the Creative Commons Attribution 4.0 International License (<http://creativecommons.org/licenses/by/4.0/>), which permits unrestricted use, distribution, and reproduction in any medium, provided you give appropriate credit to the original author(s) and the source, provide a link to the Creative Commons license, and indicate if changes were made.

References

- Maslov, K., Stoica, G., Wang, L.V.: In vivo dark-field reflection-mode photoacoustic microscopy. *Opt. Lett.* **30**(6), 625–627 (2005)
- Zhang, H.F., Maslov, K., Stoica, G., Wang, L.V.: Functional photoacoustic microscopy for high-resolution and noninvasive in vivo imaging. *Nat. Biotechnol.* **24**(79), 848–851 (2006)
- Yao, J., Wang, L.V.: Photoacoustic microscopy. *Laser Photon Rev.* **7**(5), 758–778 (2013)
- Wang, P.H., Liu, H.L., Hsu, P.H., Lin, C.Y., Wang, C.R., Chen, P.Y., Wei, K.C., Yen, T.C., Li, M.L.: Gold-nanorod contrast-enhanced photoacoustic micro-imaging of focused-ultrasound induced blood-brain-barrier opening in a rat model. *J. Biomed. Opt.* (2012). doi:[10.1117/1.JBO.17.6.061222](https://doi.org/10.1117/1.JBO.17.6.061222)
- Tsunoi, Y., Sato, S., Watanabe, R., Kawauchi, S., Ashida, H., Terakawa, M.: Compact acoustic-resolution photoacoustic imaging system with fiber-based illumination. *Jpn. J. Appl. Phys.* **53**, 126701 (2014). doi:[10.7567/JJAP.53.126701](https://doi.org/10.7567/JJAP.53.126701)
- Omar, M., Gateau, J., Ntziachristos, V.: Ultrawideband reflection-mode photoacoustic mesoscopy. *Opt. Lett.* (2006). doi:[10.1364/OL.39.003911](https://doi.org/10.1364/OL.39.003911)
- Li, M.L., Zhang, H.E., Maslov, K., Stoica, G., Wang, L.V.: Improved in vivo photoacoustic microscopy based on a virtual-detector concept. *Opt. Lett.* **31**(4), 474 (2006). doi:[10.1364/OL.31.000474](https://doi.org/10.1364/OL.31.000474)
- <https://www.advantest.com/products/leading-edge-products/wel5100>
- Kawaguchi, Y., Iwazaki, H., Ida, T., Nishi, T., Tanikawa, Y., Nitta, N.: New polymer-based phantom for photoacoustic imaging. *Proc. SPIE* **8945**, 89450A (2014). doi:[10.1117/12.2037517](https://doi.org/10.1117/12.2037517)
- Walker, H.L., Mason Jr, A.D.: A standard animal burn. *J. Trauma* **8**, 1049–1051 (1968)
- Ida, T., Kawaguchi, Y., Kawauchi, S., Iwaya, K., Tsuda, H., Saitoh, D., Sato, S., Iwai, T.: Real-time photoacoustic imaging system for burn diagnosis. *J. Biomed. Opt.* **19**, 086013 (2014). doi:[10.1117/1.JBO.19.8.086013](https://doi.org/10.1117/1.JBO.19.8.086013)
- Ida, T., Iwazaki, H., Kawaguchi, Y., Kawauchi, S., Ohkura, T., Iwaya, K., Tsuda, H., Saitoh, D., Sato, S., Iwai, T.: Burn depth assessments by photoacoustic imaging and laser Doppler imaging. *Wound Repair Regen.* **24**(2), 349–355 (2015). doi:[10.1111/wrr.12374](https://doi.org/10.1111/wrr.12374)